01 Oct 2022

Reinforcement of the Plasmon–phonon Coupling in **A**-Quartz Via Deposition of Gold Nanoparticles in Etched Ion Tracks

Maria C. Garcia Toro

Miguel L. Crespillo

Jose Olivares

Joseph T. Graham
Missouri University of Science and Technology, grahamjose@mst.edu

Recommended Citation

THE EUROPEAN
PHYSICAL JOURNAL PLUS

Regular Article

Reinforcement of the plasmon–phonon coupling in α-quartz via deposition of gold nanoparticles in etched ion tracks

Maria C. Garcia Toro[1] , **Miguel L. Crespillo**[2,3] , **Jose Olivares**[3,4] , **Joseph T. Graham**[1,a]

[1] Department of Nuclear Engineering and Radiation Science, Missouri University of Science and Technology, Rolla, MO 65409, USA
[2] Department of Material Science and Engineering, University of Tennessee, Knoxville, TN 37996, USA
[3] Centro de Micro-Análisis de Materiales (CMAM), Universidad Autónoma de Madrid, 28049 Madrid, Spain
[4] Instituto de Optica, Consejo Superior de Investigaciones Científicas (IO,CSIC), 28006 Madrid, Spain

Abstract This study reports a large reinforcement of the plasmon–phonon coupling in alpha quartz achieved through the controlled deposition of gold nanoparticles into nanotemplates produced through chemical etching of ion tracks. Preferential agglomeration of nanoparticles within the etched ion tracks (nanowells) was observed in Scanning Electron Microscopy and Atomic Force Microscopy images. Raman characterization of quartz substrates with different nanoparticle concentrations revealed a relationship between the plasmon–phonon coupling intensity and nanoparticle concentration. Reinforcement of the plasmon–phonon coupling was observed as an increase in the Raman intensity with increasing concentration of deposited nanoparticles. The intensity initially increased linearly with nanoparticle concentration up to about 4×10^6 nps/µL where a saturation regime was identified. In the saturation regime, a roughly 200-fold increase in the scattering intensity was measured in the first micron of the specimen. At higher nanoparticle concentrations, the Raman intensity decreased exponentially following the Beer–Lambert Law. The reduction in the Raman intensity is attributed to increased laser absorption with increasing nanoparticle layer thickness. Comparatively weak reinforcement of Raman scattering was observed when nanoparticles were deposited on unirradiated and unetched samples, suggesting that the reinforcement of plasmon–phonon coupling may be favored by the anisotropic geometry of the nanowells. In particular, the etched tracks promote nanoparticles agglomeration likely promoting the formation of plasmon hotspots.

1 Introduction

The incorporation of nanostructures in transparent materials presents a promising route for modifying optical properties. One of the goals of nanophotonics, for example, is to exploit photon-matter interactions at the nanometer scale in order to manipulate light at spatial scales below the diffraction limit. In nanostructured metamaterials, the effective linear and non-linear properties of an optical medium are tailored through modifications to the dielectric permittivity and through quantum confinement effects. The properties of such nanostructured optical materials can differ significantly from their bulk counterparts [1, 2].

Metallic nanostructures alter light-matter interaction through their ability to support collective electronic excitations (plasmons) [3–5]. Conduction electrons at a metal surface can be driven to oscillate by the oscillating electric field of incident electromagnetic radiation. Due to the nanometric size of such particles and the electromagnetic boundary conditions imposed by their surface, discrete surface modes called localized surface plasmons can be excited by incident light. Localized surface plasmons have been shown to enhance the optical response of materials by several orders of magnitude [6–8].

Plasmonic nanoparticles modify the phase of the electric and magnetic fields in their vicinity due to their capacity to strongly couple local electron density fluctuations with an electromagnetic field of wavelength larger than the nanoparticle itself [9]. When metallic nanoparticles are separated within a distance comparable to their diameter, additional electromagnetic effects appear [10, 11]. Plasmon coupling occurs when two or more plasmonic nanoparticles form clusters, causing their near-field surface plasmons to hybridize and further enhance the localized electric field within the clusters (hotspots). Such clusters also enable the exchange of hot electrons between adjacent nanoparticles. Previous studies have reported an enhancement of the interparticle electric field by several orders of magnitude, far exceeding the field enhancement created by a single plasmonic nanoparticle [6–8, 10, 11]. In addition to the field enhancement, hybridization shifts the surface plasmon resonance to longer wavelengths. For example, using Raman spectroscopy, it was observed that the plasmon resonance for spherical AuNPs shifted from 520 to ∼ 660 nm as the particles aggregate [12]. Surface plasmons can couple incident electromagnetic radiation (e.g. visible light) to the atomic vibrational modes

Fig. 1 SEM images of irradiated and etched Y-cut alpha quartz samples. The nanowell surface dimensions (left) and depth (right) are indicated
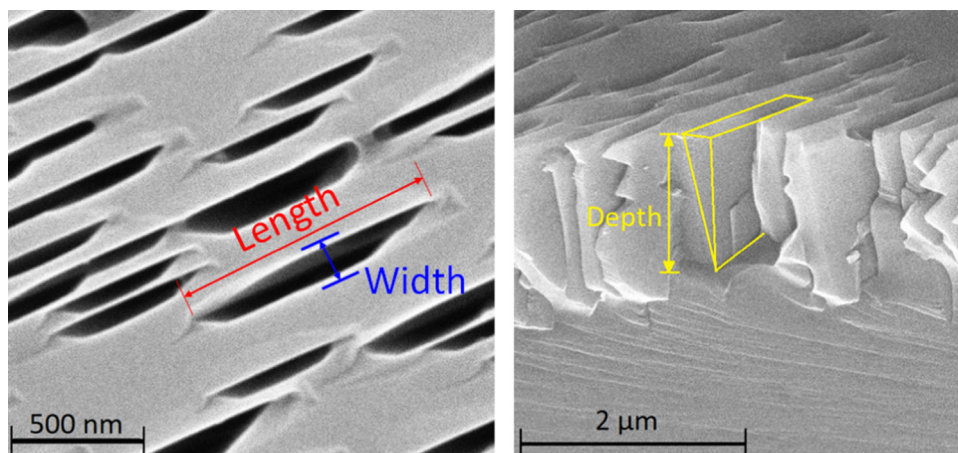
of molecules and solids. This coupling is exploited in Surface-enhanced Raman Spectroscopy (SERS) which is used to detect and characterize substances at ultra-low concentrations [13].

Recently, nanoplasmonic devices have received great interest in physics and engineering disciplines. Nanoplasmonics are expected to become a key technology that will merge electronics and conventional photonic components on the same device [4, 14, 15]. Nanoplasmonics have been used in nanoantennas [16, 17], efficient solar cells [18, 19], nanoplasmonic biosensors [20, 21], SERS [22, 23], localized heat generation [24, 25], smart coatings [26, 27], plasmonic nanofilters [28, 29], and other technologies.

Quartz is widely used in optoelectronics and photonic devices. Its optical and electrical properties, thermostability, high resistance to chemical attack, insulating and piezoelectric properties, abundance, and affordability make quartz an important technological material in applications including integrated optics, microelectronics, and spectroscopy. Developing techniques to modify the optical properties of quartz helps broaden its technological utility. Previous efforts have been made to fabricate quartz nanotemplates that can be functionalized to construct nanodevices with unique optical, thermal, and electronic properties [30]. The study included samples of Y-cut alpha quartz that were irradiated with highly energetic ions and subsequently vapor-etched with hydrofluoric acid solutions to produce and tailor anisotropic nanowell structures. In addition, the modification of the optical response of the ion-irradiated and etched nanotemplates was analyzed [31].

The main objective of the present work is to incorporate gold nanoparticles (AuNPs) into quartz nanotemplates in order to modify its optical response by reinforcing the plasmon–phonon coupling via localized surface plasmons in intimate contact with the quartz crystal structure. Gold nanoparticles with a mean diameter of 7 nm were deposited into the etched nanowells by dropping a colloidal suspension on the sample surfaces and allowing them to dry. The characterization of the resulting plasmonic material is based on scanning electron microscopy (SEM), atomic force microscopy (AFM), and Raman spectroscopy.

2 Methods

Single-side polished Y-cut alpha quartz substrates from MTI, Inc. were used. The samples were irradiated a few degrees off normal incidence with 40 MeV I^{7+} (0.31 MeV/amu) swift heavy ions to a fluence of 1×10^9 cm^{-2}, in the isolated track regime [30], in the standard beamline chamber of the Centre of Micro-Analysis of Materials (CMAM-UAM) at the University Autonoma de Madrid (UAM) [32]. When the electronic energy loss deposited by the projectile ions into the crystal overcomes the amorphization threshold ($S_{e,th}$ ~ 2–4 keV/nm) [33], the passage of the ions forms ion tracks, highly disordered or amorphous columnar structures with nanometer diameters that extend several microns into the substrate. After irradiation, the samples were vapor-etched with an aqueous solution of 20%w HF for 1 h at room temperature. The resulting nanostructures had anisotropic nanochannel or nanowell shapes with superficial dimensions of ~ 600 nm in length and ~ 200 nm in width, and depths up to ~ 1 μm [30]. Various well/channel shapes and aspect ratios are possible through the crystallographic-direction-dependent etching rate, choice of crystal cut, and etchant conditions. Figure 1 shows SEM images of the nanowell templates used in this study. The micrograph on the left shows the superficial nanowell openings on the sample surface; the micrograph on the right shows an edge-on cross-section of a cleaved sample where the nanowell depth can be observed. SEM micrographs were obtained at a high voltage of 15 kV, with a current of 86 pA, a working distance of 4.1 mm, and magnifications ranging between 20,000 × and 50,000 × . The samples were coated with a 3 nm layer of Au/Pd to inhibit charging, reduce thermal damage, and improve the secondary electron signal required for the topographic examination.

Citrate-coated AuNPs with spherical shape and 7 nm diameter were used in the deposition. The AuNPs were purchased from Luna Nanotech as a liquid suspension in water (1.55×10^{-6} M). The citrate coating acts as a stabilizing surfactant to avoid agglomeration (size dispersity: ~ 1.2 nm). The AuNPs deposition on the sample surfaces was conducted by dripping 20 μL drops of a dilute

suspension (2.3×10^{-8} M in deionized water) onto the samples and letting them dry in air. Samples with different areal concentrations of deposited AuNPs were prepared by varying the number of drops. Before depositing a new drop, the sample surface was cleaned by rinsing with deionized water to remove the nanoparticles that were not trapped inside the nanowells. This procedure was used to produce specimens where most of AuNPs reside inside the nanowells.

Raman spectra were acquired with a Horiba Xplora Plus Confocal Raman Microscope at room temperature with a 785 nm semiconductor laser. Spectra were collected using a $10 \times$ objective lens with an air numerical aperture of 0.25, 1800 lines mm^{-1} grating, and a 100 μm diameter pinhole. Based on these parameters, the index of refraction of quartz and the formulae in ref. [34], an optical sectioning resolution (FWHM) of about 98.4 μm is assumed. All measurements were acquired in the backscattering geometry without polarization optics.

SEM images were taken to characterize the distribution of AuNPs after deposition. Micrographs were acquired at high voltage (10 kV), with a current of 43 pA, a working distance of 5.3 mm, and magnifications ranging between $20,000 \times$ and $50,000 \times$. To inhibit charging and improve the secondary electron signal, the samples were coated with a 15 nm layer of carbon. Carbon was used instead of Au/Pd coating to avoid interference between the AuNPs and the conductive coating layer.

3 Results and discussion

Figure 2 (left) shows an SEM micrograph of a sample with AuNPs deposited at a low concentration (4×10^6 nps/μL). Agglomeration of AuNPs was observed in the SEM image. This is expected as capillary forces draw NPs together as solvent evaporization takes place. Most of the agglomerated AuNPs were found inside the nanowells. At low concentrations, AuNPs were not homogeneously distributed within the nanowells. Some wells/channels had a high-density AuNPs while others were empty or nearly so. Also, some of the nanowells were not completely filled to the surface. This provides some evidence that through some combination of the anisotropic nanowells geometry and direction of capillary forces, most of the AuNPs tend to agglomerate at the bottom of the wells. Figure 2 (right) shows AFM surface profiles of a nanowell filled with a low concentration of AuNPs. A comparison of line scans A, B and C shows the presence of a large agglomerate in the center of a wide (~ 200 nm) channel. It is important to note that despite the apparent morphological differences between the SEM images in Figs. 1 and 2, both substrates were irradiated and etched under the same conditions. The morphological differences are attributed, in part, to the different coatings used to obtain each image (AuPd for Fig. 1 and carbon for Fig. 2). It also seems that there was some heterogeneity in the etching rate across the surface of each specimen. The heterogeneity did not affect the Raman measurements which were averaged over a macroscopic area.

Despite the non-uniform distribution of AuNPs, a clear modification in the Raman response of quartz by the presence of hotspots in agglomerated AuNPs was observed. The reinforcement of the electromagnetic field due to plasmon oscillations can occur between as few as two coupled nanoparticles [4–9, 35, 36]. Figure 3 shows the Raman spectra of samples with different nanoparticle concentrations. The spectrum of a sample with no AuNPs was included for comparison purposes. A detailed description of the Raman spectrum of quartz can be found in Refs. [37–39].

A significant change in the Raman scattering intensities was observed in samples with deposited AuNPs. Samples with a low concentration (up to 4×10^6 nps/μL) of AuNPs exhibited a linear increase in the Raman scattered intensity with concentration. However, at higher concentrations, the Raman intensity decreased with increasing concentration. These observations suggest that as AuNP coverage increases, AuNPs cluster within the nanowells forming a large number of hotspots in close proximity to the quartz structure, thereby enhancing the Raman response. With continued deposition, however, AuNPs begin to cover the sample surface, blocking underlying hotspots formed near the quartz with an absorbing layer of gold. This results in a saturation of the SERS signal and, with continued deposition of AuNPs, light absorption. In other words, the large number of nanoparticles at the surface increases the mass thickness of gold between the incident laser and the quartz substrate to the point where significant attenuation prevents incident light from reaching the substrate.

Figure 4 shows the relationship between the enhancement in the total Raman intensity (integrated Stokes spectrum) with AuNP concentration. The enhancement factor was evaluated by comparing the measured intensity of the coated samples with the intensity obtained from the samples without AuNPs, calculated as shown in Eq. (1):

$$\text{EF} = \frac{I}{I_0} \tag{1}$$

where I is the Raman intensity obtained after depositing AuNPs and I_0 is the Raman intensity obtained without AuNPs. It is important to note that the Raman microscope conditions were kept unmodified for all measurements. At lower concentrations, a linear relationship between the EF with the AuNPs concentration was clearly observed suggesting that the enhancement scales with the number of nanoparticles in the nanowells (see Fig. 4 inset). A maximum EF = 3.41 was observed at 4×10^6 nps/μL. It should be noted, however, that the depth of the wells represents only 1% of the optical sectioning resolution used in the Raman measurements. Assuming that the Raman susceptibility of the quartz below the template layer is unaffected, there is an approximately $240 \times$ increase in the Raman scattering intensity in the upper 1 μm of the specimens at the optimum AuNP concentration.
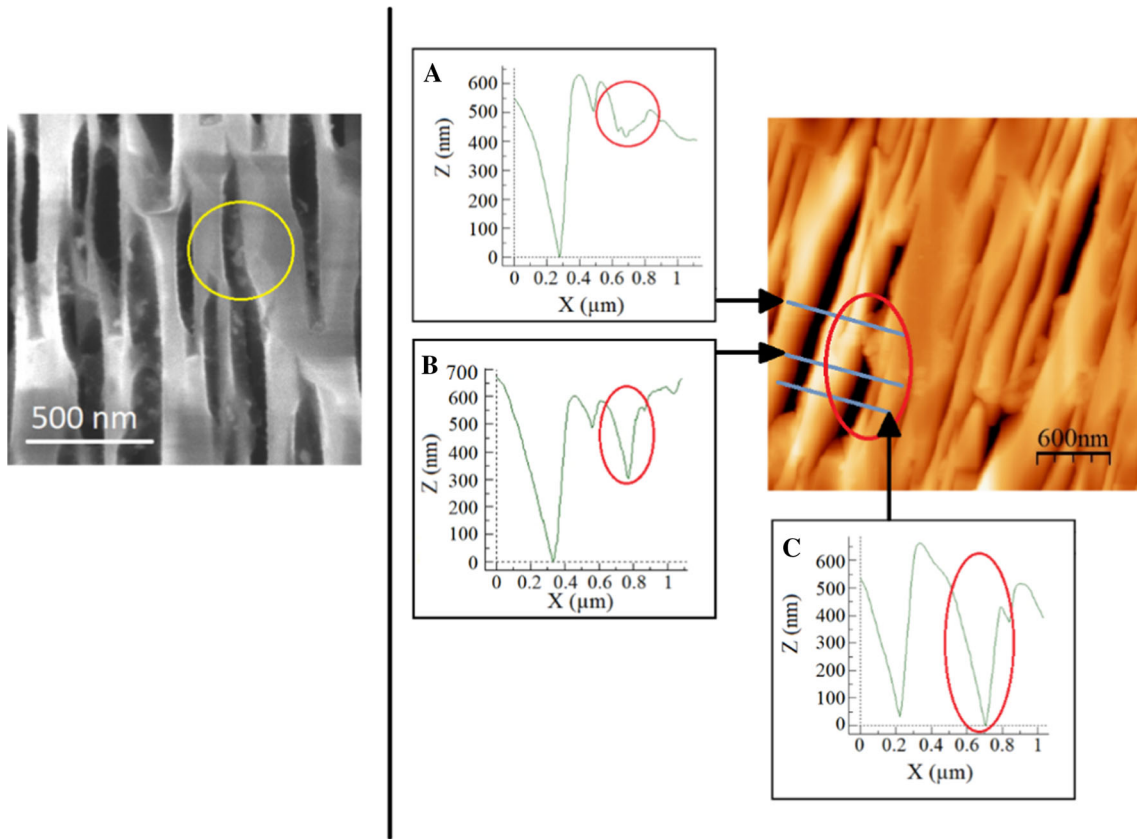
Fig. 2 (Left) SEM micrograph a sample with deposited AuNPs. (Right) AFM line scan depth profiles of a nanowell with deposited AuNPs
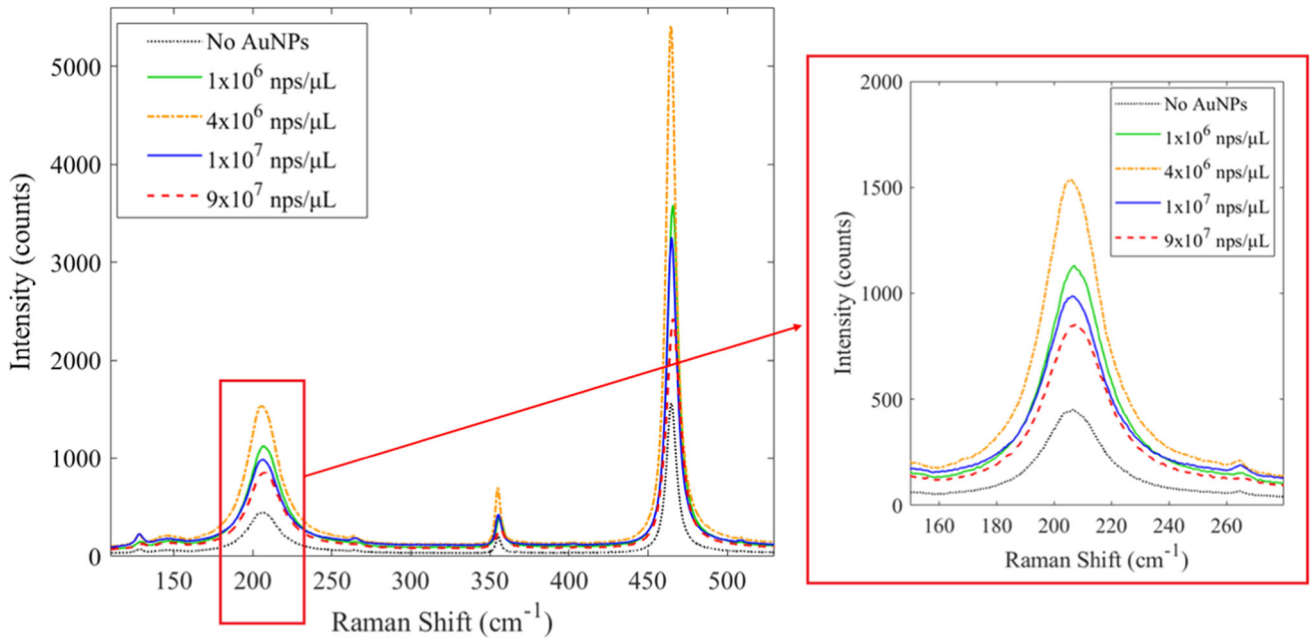

Fig. 3 Raman spectra of samples with different AuNP concentrations

In the regime of light attenuation, after the maximum enhancement factor is reached, the scattering intensity can be compared to the Beer–Lambert Law, shown in Eq. (2):

$$\frac{I}{I_0} = e^{-\mu x} \tag{2}$$

Fig. 4 Raman enhancement factor vs. AuNPs concentration. Circles and squares represent the experimental data. The inset shows the lower NPs concentration regime
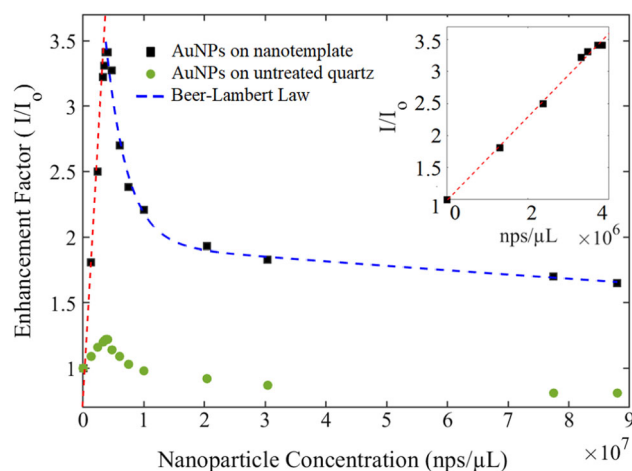
μ is the molar extinction coefficient (1.1×10^7 M^{-1} cm^{-1}) of the AuNPs, provided by Luna Nanotech, and x, the molar areal concentration, was assumed to be proportional to the nanoparticle concentration.

The Beer-Lambert Law from Eq. 2 is overlayed on the data in Fig. 4 with an additive background constant to account for areas of the quartz between the channels/wells. The Beer-Lambert law shows good agreement with experimental data suggesting that the attenuation of the Raman signal at the higher concentrations is indeed the result of laser light absorption.

Figure 4 also shows the effect of depositing AuNPs on unirradiated, unetched (untreated) quartz substrates. Only a small enhancement effect was observed from the particle lying on the surface of the substrate. However, the effect was only seen in a narrow range of low concentrations before absorption effects diminish the signal. Evidently, the wells/channels greatly enhance the SERS response.

It should be noted that the Raman measurements were performed off-resonance. The surface plasmon resonance of AuNPs occurs around 520 nm for sub-50 nm particles [40]. For isolated (non-hybridized) AuNPs, a standard 532 nm laser found on many Raman systems is well suited for characterization. As hotspots form and plasmons hybridize, however, the resonance shifts to longer wavelengths and Raman measurements taken using a pump wavelength significantly longer than 520 nm (i.e. within the low energy tail of the resonance) can be expected to exhibit an enhancement due solely to the redshift. Thus, the observed Raman enhancement seen in these data could have its origins in the local field enhancement around hotspots, the redshift from hybridization, or a combination of both.

Tian et al. [12] compared the SERS signals of unaggregated and aggregated spherical AuNPs using an organic dye as a probe at both 532 nm and 785 nm laser wavelengths. They did not observe a significant SERS signal from the unaggregated particles when measured with the 532 nm laser (near-resonance). As the particles aggregated, however, a notable enhancement in the 785 nm Raman spectrum was observed. The enhancement could be attributed, in part to the redshift from 520 to 660 nm that brought the resonance closer to the 785 nm wavelength of the laser, and in part to the local field enhancement from the hotspots. However, given that the authors reported a significantly stronger enhancement of the SERS signal in the aggregated (hybridized) NPs *off-resonance*, one can conclude that the local field enhancement effect is likely dominant. Given the similarity of the phenomena examined in Tian et al. and those presented in this work, it is hypothesized that the main contribution to the observed enhanced Raman signal in the nanowells is the local field enhancement from hotspots. Further insight into the relative contributions of the redshift and local field enhancement effects might be obtained by repeating these Raman measurements at 532 nm and at an intermediate wavelength (e.g. 638 nm). Indeed, such measurements, if performed *in-situ* might provide additional valuable information on the clustering process within the wells as it occurs.

4 Conclusions

A plasmonic material was fabricated using ion irradiation, wet etching and nanoparticle deposition that exhibited plasmon–phonon coupling behaviour. Raman microscopy revealed two regimes in the optical response. In the first, a linear enhancement of the Raman scattering intensity was observed with increasing AuNP concentrations, up to 4×10^6 nps/μL. A maximum enhancement factor of 3.4 was observed corresponding to a roughly 200-fold enhancement of the optical response within the nanowells. In the regime of higher nanoparticle concentrations, an exponential reduction in the Raman intensity from light absorption in the AuNPs followed the Beer-Lambert Law. Similar enhancement behaviour was not seen in the spectra from unirradiated and unetched quartz when nanoparticles were deposited. These anisotropic nanostructures may be used to efficiently couple light to optical phonons near the surface of quartz via localized surface plasmons. Ion beam irradiation, chemical etching, and nanoparticle deposition have many tunable parameters, making these techniques flexible tools for tailoring the properties of novel photonic devices.

Data Availability Statement This manuscript has associated data in a data repository. [Authors' comment: The data that support the findings of this study are available from the corresponding author upon reasonable request.]

Declarations

Conflict of interest The authors have no competing interests to disclose.

References

1. P. Kumbhakar, S.S. Ray, A.L. Stepanov, J. Nanomater. **2014**, 181365 (2014). https://doi.org/10.1155/2014/181365
2. M.L. Brongersma, V.M. Shalaev, Science **328**, 440 (2010). https://doi.org/10.1126/science.1186905
3. W.L. Barnes, A. Dereux, T.W. Ebbesen, Nature **424**, 824 (2003). https://doi.org/10.1038/nature01937
4. N.J. Halas, Nano Lett. **10**, 3816 (2010). https://doi.org/10.1021/nl1032342
5. W.A. Murray, W.L. Barnes, Adv. Mater. **19**, 3771 (2007). https://doi.org/10.1002/adma.200700678
6. T. Chen, M. Pourmand, A. Feizpour, B. Cushman, B.M. Reinhard, J. Phys. Chem. Lett. **4**, 2147 (2013). https://doi.org/10.1021/jz401066g
7. T. Chung, Y. Lee, M. Ahn, W. Lee, S. Bae, H. Hwang, K. Jeong, Nanoscale **11**, 8651 (2019). https://doi.org/10.1039/C8NR10539A
8. Y. Sonnefraud, A.L. Koh, D.W. Mccomb, S.A. Maier, Laser Photonics Rev. **6**, 277 (2012)
9. P.K. Jain, M.A. El-sayed, Chem. Phys. Lett. **487**, 153 (2010). https://doi.org/10.1016/j.cplett.2010.01.062
10. A. Lereu, R.H. Farahi, L. Tetard, S. Enoch, T. Thundat, A. Passian, Opt. Express **21**, 12145 (2013). https://doi.org/10.1364/OE.21.012145
11. N. Zohar, L. Chuntonov, G. Haran, J. Photochem. Photobiol. C **21**, 26 (2014). https://doi.org/10.1016/j.jphotochemrev.2014.10.002
12. F. Tian, F. Bonnier, A. Casey, A.E. Shanahana, H.J. Byrne, Anal. Methods **6**, 9116 (2014). https://doi.org/10.1039/C4AY02112F
13. R. Pilot, R. Signorini, C. Durante, L. Orian, M. Bhamidipati, L. Fabris, Biosensors **9**, 57 (2019). https://doi.org/10.3390/bios9020057
14. Z. Liang, J. Sun, Y. Jiang, L. Jiang, Plasmonics **9**, 859 (2014). https://doi.org/10.1007/s11468-014-9682-7
15. E. Ozbay, Science **311**, 189 (2006). https://doi.org/10.1126/science.1114849
16. X. Ni, N.K. Emani, A.V. Kildishev, A. Boltasseva, V.M. Shalaev, Science **335**, 427 (2012). https://doi.org/10.1126/science.1214686
17. V. Giannini, A.I. Fernández-Domínguez, S.C. Heck, S.A. Maier, Chem. Rev. **111**, 3888 (2011). https://doi.org/10.1021/cr1002672
18. S. Pillai, M.A. Green, Sol. Energy Mater. Sol. Cells **94**, 1481 (2010). https://doi.org/10.1016/j.solmat.2010.02.046
19. P. Reineck, G.P. Lee, D. Brick, M. Karg, P. Mulvaney, U. Bach, Adv. Mater. **24**, 4750 (2012). https://doi.org/10.1002/adma.201200994
20. G.A. Lopez, M.C. Estevez, M. Soler, L.M. Lechuga, Nanophonics **6**, 123 (2017). https://doi.org/10.1515/nanoph-2016-0101
21. A.H. Nguyen, S.J. Sim, Biosens. Bioelectron. **67**, 443 (2015). https://doi.org/10.1016/j.bios.2014.09.003
22. J.B. Jackson, N.J. Halas, Proc. Natl. Acad. Sci. **101**, 17930 (2004). https://doi.org/10.1073/pnas.0408319102
23. P.P. Patra, R. Chikkaraddy, R.P.N. Tripathi, A. Dasgupta, G.V.P. Kumar, Nat. Commun. **5**, 4357 (2014). https://doi.org/10.1038/ncomms5357
24. U. Guler, J.C. Ndukaife, G.V. Naik, A.G.A. Nnanna, A.V. Kildishev, V.M. Shalaev, A. Boltasseva, Nano Lett. **13**, 6078 (2013). https://doi.org/10.1021/nl4033457
25. G. Baffou, J. Polleux, H. Rigneault, S. Monneret, J. Phys. Chem. C **118**, 4890 (2014). https://doi.org/10.1021/jp411519k
26. Q. Hao, W. Li, H. Xu, J. Wang, Y. Yin, H. Wang, L. Ma, F. Ma, X. Jiang, O.G. Schmidt, P.K. Chu, Adv. Mater. **30**, 1705421 (2018). https://doi.org/10.1002/adma.201705421
27. A. Tittl, X. Yin, H. Giessen, X.-D. Tian, C. Kremers, D.N. Chigrin, N. Liu, Nano Lett. **13**, 1816 (2013). https://doi.org/10.1021/nl4005089
28. Y. Leroux, J.C. Lacroix, C. Fave, V. Stockhausen, N. Félidj, J. Grand, A. Hohenau, J.R. Krenn, Nano Lett. **9**, 2144 (2009). https://doi.org/10.1021/nl900695j
29. M. Ye, L. Sun, X. Hu, B. Shi, B. Zeng, L. Wang, J. Zhao, S. Yang, R. Tai, H.-J. Fecht, J.-Z. Jiang, D.-X. Zhang, Opt. Lett. **40**, 4979 (2015). https://doi.org/10.1364/OL.40.004979
30. M.C. Garcia Toro, M.L. Crespillo, J. Olivares, J.T. Graham, Nucl. Inst. Methods Phys. Res. B **498**, 52 (2021). https://doi.org/10.1016/j.nimb.2021.04.013
31. M.C. Garcia Toro, M.L. Crespillo, J. Olivares, J.T. Graham, J. Raman Spectrosc. **52**, 1185 (2021). https://doi.org/10.1002/jrs.6108
32. A. Redondo-Cubero, M.J.G. Borge, N. Gordillo, P.C. Gutiérrez, J. Olivares, R. Pérez Casero, M.D. Ynsa, Eur. Phys. J. Plus (2021). https://doi.org/10.1140/epjp/s13360-021-01085-9
33. O. Peña-Rodríguez, J. Manzano-Santamaría, A. Rivera, G. García, J. Olivares, F. Agulló-López, J. Nucl. Mater. **430**, 125 (2012). https://doi.org/10.1016/j.jnucmat.2012.07.001
34. T. Wilson, J. Microsc. **244**, 113 (2011). https://doi.org/10.1111/j.1365-2818.2011.03549.x
35. H. Yu, Q. Sun, J. Yang, K. Ueno, T. Oshikiri, A. Kubo, Y. Matsuo, Q. Gong, H. Misawa, Opt. Express **25**, 6883 (2017). https://doi.org/10.1364/OE.25.006883
36. J.A. Schuller, E.S. Barnard, W. Cai, Y.C. Jun, J.S. White, M.L. Brongersma, Nat. Mater. **9**, 193 (2010). https://doi.org/10.1038/nmat2630
37. B.D. Saksena, Proc. Indian Acad. Sci. Sect. A **12**, 93 (1940). https://doi.org/10.1007/BF03170730
38. J.F. Scott, S.P.S. Porto, Phys. Rev. **161**, 903 (1967). https://doi.org/10.1103/PhysRev.161.903

39. P. Umari, A. Pasquarello, A. Dal Corso, Phys. Rev. B Condens. Matter Mater. Phys. **63**, 1 (2001). https://doi.org/10.1103/PhysRevB.63.094305
40. Y. Qiu He, S. Pu Liu, L. Kong, Z. Fang Liu, Spectrochim. Acta Part A Mol. Biomol. Spectrosc. **61**, 2861 (2005). https://doi.org/10.1016/j.saa.2004.10.035